

Use of 4×4 transfer matrix method in the study of surface magnon polaritons via simulated attenuated total reflection measurements on the antiferromagnetic semiconductor MnF_2

Nathan Hale , Ingve Simonsen , Christoph Brüne , and Morten Kildemo 

Department of Physics, NTNU–Norwegian University of Science and Technology, NO-7491 Trondheim, Norway

 (Received 27 September 2021; revised 1 February 2022; accepted 4 March 2022; published 22 March 2022)

The surface magnon polaritons (SMPs) present in thin film antiferromagnet semiconductors can be extremely confined, having most of their energy distributed within the magnetic medium. For extremely thin films these SMPs can therefore be well described using a quasimagnetostatic treatment. In this work Berreman's 4×4 transfer matrix method (TMM) is used to study the SMPs supported by thicker films, beyond the magnetostatic approximation. Focus is placed on the antiferromagnet semiconductor MnF_2 for which attenuated total reflection measurements are modeled, probing the hyperbolic dispersion of the medium. The dispersion relations from both the TMM and the analytical quasimagnetostatic approximation are compared. For thicker films, the coupling efficiencies into the SMP energy channels are analyzed as a function of air gap distances. The TMM is used to probe the SMP dispersion for realistic experimental configurations with modifications including type of substrate, film thickness, and crystal axis orientation. Rich phenomena are observed such as strong SMP-waveguide mode coupling and SMPs with negative refraction.

DOI: [10.1103/PhysRevB.105.104421](https://doi.org/10.1103/PhysRevB.105.104421)

I. INTRODUCTION

Antiferromagnetic materials provide interesting candidates for spintronics owing to their resonances in the THz regime [1]. These materials could add to the development of novel spintronic devices such as spin filters, spin diodes, and magnon transistors [2,3]. Future THz communications will require efficient ways of coupling electrons and light, or even magnons and light. The current state of electronics and optoelectronic devices has heavily relied on the establishment of optical methods for characterization, monitoring, and control of semiconductors. As such, in order for advances in spintronics it is necessary to establish optical characterization methods and the underlying appropriate modeling for establishing these.

The realization of materials confining and enhancing electric fields over subwavelength length scales has given the field of plasmonics considerable attention. Specifically the utilization of surface plasmon polaritons (SPPs) has opened up novel avenues of research for applications in optical sensing, light emission, and subdiffractional imaging and focusing [4–9]. Due to the duality of Maxwell's equations [10], modes analogous to SPPs can be excited in magnetic media. These surface spin waves, also known as surface magnon polaritons (SMPs), arise at the interfaces between materials with a positive real component of the permeability $\text{Re}(\mu)$ and films and bulk media with negative $\text{Re}(\mu)$ [11,12]. A basic description of a SMP is that of a quasiparticle that partitions its energy between electron-spin waves in the magnetic medium and electromagnetic fields in the adjacent dielectric medium. The majority of materials with negative $\text{Re}(\mu)$ fall into two categories, uniaxial semiconductors with antiferromagnetic resonances in the terahertz and engineered split-ring resonator metamaterials

with resonances at optical frequencies [13,14]. Antiferromagnetic resonances have been investigated in semiconductors including GdAlO_3 , FeF_2 , and MnF_2 [15–17]. Gaining control of the SMPs supported by antiferromagnetic semiconductors could offer numerous applications in the rising field of spintronics [18].

This work will focus on the semiconductor MnF_2 , which becomes antiferromagnetic at temperatures below its Néel temperature T_N [19]. A diverse range of SMPs is supported by single-crystal MnF_2 . For example, bulk MnF_2 supports single-mode SMPs which become nonreciprocal with the introduction of an applied magnetic field [20]. Moreover, MnF_2 thin films have been shown to support multiple branched quasimagnetostatic modes with extreme confinement factors [21]. The Lorentzian nature of the antiferromagnetic resonance present in MnF_2 means the SMPs it supports are less analogous to SPPs, which have a Drude-like permittivity and are more resemblant of surface phonon polaritons (SPhPs), owing to the anisotropic nature of their tensorial permittivity. SPhPs have resonances in the mid-infrared and have been studied on polar insulators including SiC [22] and α -quartz [23] as well as on graphene in the case of ultrathin films [24]. Due to their Lorentzian-like dispersion, SMPs and SPhPs only exist within a frequency range in which the transverse components of $\text{Re}(\mu)$ and $\text{Re}(\epsilon)$ are respectively negative. These frequency regions are known as restrahlen bands owing to their reflective effects. The limited range of these bands means coupling into SMP modes requires operating with narrower bandwidths than that with the SPPs supported by Drude-like metal surfaces. MnF_2 , like other antiferromagnetic semiconductors, has a uniaxial permeability at THz frequencies for s -polarized light. The optical axis of the crystal is indicated by a Néel vector \vec{N} as seen in Fig. 1(a). For frequencies within the

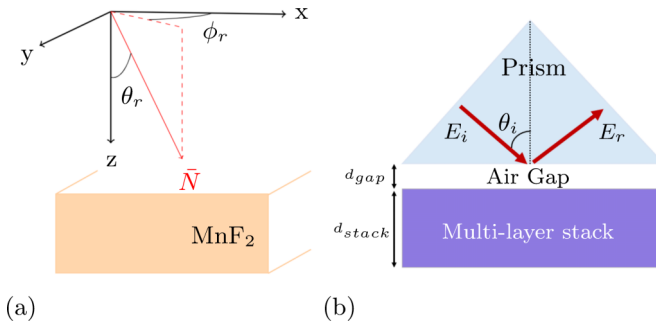


FIG. 1. (a) The coordinate system for a MnF_2 thin film. The Euler rotation angles θ_r and ϕ_r indicate the direction of the antiferromagnetic Néel vector \vec{N} (in red). (b) An Otto configuration for an ATR measurement. An air gap separates the high-index prism from a SMP-supporting multilayer stack. The incident and reflected electric fields are shown by E_i and E_r , with a polar incidence angle θ_i . The air gap and stack thicknesses are indicated by d_{gap} and d_{stack} , respectively.

restrahlen band, the real components of permeability parallel and normal to the surface will have opposite signs. This is known as hyperbolic dispersion and allows for the propagation of otherwise evanescent, high spatial frequency features through the medium [9].

The dispersion relation for simple SPP systems is derived by matching the transverse electric and magnetic fields on either side of an interface (or multiple interfaces) and by assuming propagating solutions parallel to the surface and decaying solutions normal to the surface. For systems including multiple layers and anisotropic materials this method can become complex. An alternative method is to find the Fresnel reflection amplitudes, where the poles correspond to eigenstates of the system [25]. In other words these poles correspond to the modes of the system that exist even when there is an infinitesimal input field. These modes correspond to guided, leaky, or surface modes. To find the reflection amplitudes of systems of anisotropic media within a stack of multiple films at arbitrary incident angles, a 4×4 transfer matrix method (TMM) must be used. In this work Berreman's 4×4 formalism will be employed which used the basis $[E_x, H_y, E_y, -H_x]^T$ [26].

The outline of this paper is as follows: The quasimagnetostatic dispersion relation for MnF_2 thin films is derived and superposed with simulated solutions from Berreman's TMM. The matrix formalism will then simulate attenuated total reflection measurements for films of thickness where the quasimagnetostatic approximation is no longer valid. The coupling efficiency between the light undergoing total internal reflection and the MnF_2 film is analyzed for each mode of the multiple branches of the hyperbolic system. Field profiles are then investigated inside and outside the MnF_2 films. Alterations to the system are then investigated including the addition of various substrate materials, different crystal axis rotations, as well as the thickness of the MnF_2 thin film. These alterations are specifically chosen to explore the SMPs supported by realistic and complex thin-film stack systems. This is in contrast to the ideal antiferromagnetic thin films and semi-infinite systems more frequently studied. Moreover,

some of the chosen systems have complex anisotropy and cannot accordingly be modeled by non- 4×4 TMMs. The intention of the paper is to gain control of spin waves for spintronic and THz communication applications by monitoring changes to the SMP's dispersion in these more complex thin-film stacks.

II. THEORY

A. Quasimagnetostatic approximation

The quasimagnetostatic approximation implies the magnetic field is curl-less, i.e., $\vec{\nabla} \times \vec{H} = 0$. This, combined with a uniaxial $\vec{\mu}$ and plane wave solutions, leads to the Walkers equation [27,28]

$$\mu(\omega)(k_x^2 + k_y^2) = -k_z^2, \quad (1)$$

where $\mu(\omega)$ is the in-plane component of the permeability tensor and k_x , k_y , and k_z are the wave vector components within the magnetic medium. This assumes both the medium has $\epsilon = 1.0$ and the film's optical axis is normal to its surfaces, as seen in Fig. 1. Focus should be placed on the necessity of the in-plane wave vector component k_x (assuming $k_y = 0$) being complex. In a lossless medium, plane waves are considered homogeneous as the planes of constant phase and amplitude are equal to one another. In a medium with loss [in this case complex $\mu(\omega)$], plane waves are considered inhomogeneous as the planes of constant phase and amplitude can differ. At an interface in a stack, however, the phase and transverse field components must be continuous. A consequence of this is the complex form of Snell's law (valid for a single polarization): $n_1 \sin(\theta_1) = n_2 \sin(\theta_2)$, where n_1 and n_2 are the refractive indices of a lossless and lossy medium, respectively, while θ_1 and θ_2 are the incident and refracted angles. In order for this condition to be fulfilled when n_2 is complex, θ_2 must also be complex. Considering the in-plane wave vector $[k_x = n_2 \sin(\theta_2) \frac{\omega}{c}]$ is the product of 2 complex values, it is itself a complex quantity. The imaginary component of k_x is strongly dependent on the imaginary component of $\mu(\omega)$ as both n_2 and θ_2 also depend on $\mu(\omega)$. Note that ω could have been chosen to be complex instead of k_x . A complex wave vector was chosen as the SMP's spatial as opposed to its temporal decay is of more interest. The magnetic analog for the dispersion relation for SPPs in conducting thin films placed in air is [29]

$$\tan\left(\frac{dk_{z2}}{2}\right) = -i \frac{k_{z2}}{\mu(\omega)k_{z1}}, \quad (2)$$

where k_{z2} and k_{z1} are components of the \vec{k} vectors normal to the surface, inside and outside the film, respectively, and d is the thickness of the film. The Néel vector is assumed to be along the z axis, normal to the surface. Combining Eqs. (1) and (2) and assuming no contribution from k_y yields an approximation for the SMP dispersion of the system

$$k_x = \frac{2}{d\sqrt{-\mu(\omega)}} \left[\tan^{-1}\left(\frac{1}{\sqrt{-\mu(\omega)}}\right) + \frac{n\pi}{2} \right], \quad (3)$$

in which k_x is the in-plane wave vector and n is the mode index. It follows from antiferromagnetic theory that $\mu_{zz} = 1$

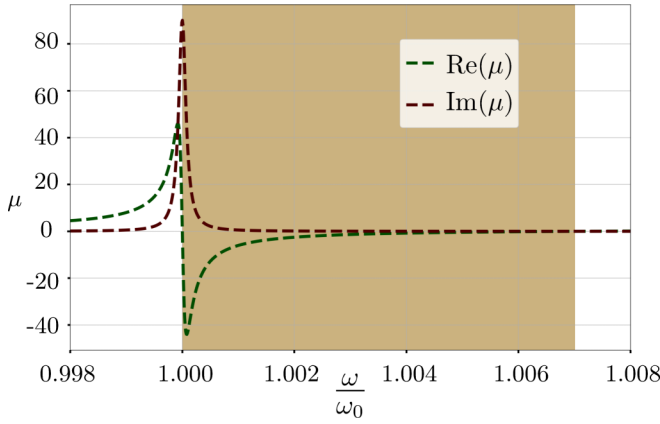


FIG. 2. The in-plane relative magnetic permeability of MnF_2 , with the real and imaginary components coloured in green and red, respectively. The region in which SMPs exist (restrahlen band) is shaded in brown.

and $\mu_{xx} = \mu_{yy} = \mu(\omega)$ with a dependence given by [30]

$$\mu(\omega) = 1 + \frac{2\mu_0\gamma^2 B_a M_s}{\omega_0^2 - (\omega + i\Gamma)^2}, \quad \bar{\boldsymbol{\mu}} = \begin{bmatrix} \mu(\omega) & 0 & 0 \\ 0 & \mu(\omega) & 0 \\ 0 & 0 & 1 \end{bmatrix}, \quad (4)$$

where the gyromagnetic ratio $\gamma/2\pi c = 0.975 \text{ cm}^{-1}/\text{T}$, the anisotropy field $B_a = 0.787 \text{ T}$, the sublattice magnetization $M_s = 6.0 \times 10^5 \text{ A/m}$, the resonant frequency $\omega_0/2\pi c = 8.94 \text{ cm}^{-1}$, the magnon damping term being $\Gamma/2\pi c = 0.0007 \text{ cm}^{-1}$, and μ_0 being the permeability of free space [31,32]. Note that c represents the speed of light in vacuum. This produces a Lorentzian line shape with a small restrahlen band on the order of GHz as seen in Fig. 2.

B. Berreman's 4×4 transfer matrix method

The quasimagnetostatic approximation will be verified and expanded upon through the use of Berreman's 4×4 transfer matrix formalism, similar to Schubert's method [33]. A 4×4 formalism is required as rotated crystal axes will result in polarization coupling which 2×2 methods cannot model [34]. This method uses Maxwell's equations and the constitutive relations to produce a matrix wave equation

$$\frac{\partial}{\partial z} \begin{bmatrix} E_x \\ H_y \\ E_y \\ -H_x \end{bmatrix} = i \frac{\omega}{c} \bar{\mathbf{\Delta}} \begin{bmatrix} E_x \\ H_y \\ E_y \\ -H_x \end{bmatrix}. \quad (5)$$

The matrix $\bar{\mathbf{\Delta}}$ has eigenvalues dictating the propagation within a layer and whose entries depend on the permittivity, permeability, bianisotropic tensors, as well as incident k vectors as outlined in Berreman's original paper. Solutions for the transverse fields as a function of z through each layer $\boldsymbol{\psi}(z)$ then depend on a partial transfer matrix $\bar{\mathbf{P}}$ which takes on an exponential form

$$\boldsymbol{\psi}(z) = \bar{\mathbf{P}}\boldsymbol{\psi}(0) = \exp(ik_0\bar{\mathbf{\Delta}}z)\boldsymbol{\psi}(0), \quad (6)$$

where $\boldsymbol{\psi}(z)$ is a dimensionless column vector containing the transverse electric and magnetic fields as a function of z , given as

$$\boldsymbol{\psi}(z) = [E_x(z), H_y(z), E_y(z), -H_x(z)]^T. \quad (7)$$

There are multiple approaches to numerically solve the matrix exponential. Common methods include using power series expansion for small layer thicknesses or the often used algorithm proposed by Wohler [35]. Despite offering computational efficiency, the Wohler method can lead to singularities for specific cases [36]. In this work, Eq. (6) is solved by determining the eigensystem of each layer, constructing a partial transfer matrix $\bar{\mathbf{P}}_i$ for each layer which can be deconstructed as

$$\bar{\mathbf{P}}_i = \bar{\mathbf{A}}_i \bar{\mathbf{K}}_i(z) \bar{\mathbf{A}}_i^{-1}, \quad (8)$$

where $\bar{\mathbf{A}}_i$ is a matrix whose columns are the eigenvectors of $\bar{\mathbf{\Delta}}_i$ and $\bar{\mathbf{K}}_i$ is a diagonal matrix whose entries are $\exp(ik_0\lambda_{i,j}z)$ in which $\lambda_{i,j}$ represents the j th eigenvalue of $\bar{\mathbf{\Delta}}_i$. By repeating this method for all the films in a system, a transfer matrix can be made for the whole stack

$$\bar{\mathbf{P}}_T = \bar{\mathbf{P}}_n(d_n)\bar{\mathbf{P}}_{n-1}(d_{n-1})\dots\bar{\mathbf{P}}_2(d_2)\bar{\mathbf{P}}_1(d_1), \quad (9)$$

where d_n is the thickness of the n th film. By also projecting the fields into the ambient (\mathbf{A}_{amb}) and substrate (\mathbf{A}_{sub}), a full transfer matrix can be made

$$\bar{\mathbf{T}} = \bar{\mathbf{A}}_{\text{amb}}^{-1} \bar{\mathbf{P}}_T^{-1} \bar{\mathbf{A}}_{\text{sub}}. \quad (10)$$

As this full transfer matrix relates the incident and reflected field amplitudes of the full system, reflection amplitudes can then be defined,

$$r_{pp} = \frac{T_{23}T_{31} - T_{21}T_{33}}{T_{13}T_{31} - T_{11}T_{33}}, \quad r_{sp} = \frac{T_{13}T_{21} - T_{11}T_{23}}{T_{13}T_{31} - T_{11}T_{33}}, \\ r_{ps} = \frac{T_{33}T_{41} - T_{31}T_{43}}{-T_{13}T_{31} + T_{11}T_{33}}, \quad r_{ss} = \frac{T_{13}T_{41} - T_{11}T_{43}}{T_{13}T_{31} - T_{11}T_{33}}. \quad (11)$$

As this 4×4 TMM is essentially 1-dimensional, simulations can be computed with high speed. This is a major advantage over techniques with more numeric complexity such as finite-difference time domain and finite-element methods which would take orders of magnitude longer time when sweeping over parameters such as frequency and wave vector. The computational efficiency and accuracy of the TMM can be used to verify results from these more numerically complex techniques. Moreover, as the method can accommodate tensors for all bianisotropic responses ($\bar{\boldsymbol{\epsilon}}$, $\bar{\boldsymbol{\mu}}$, $\bar{\boldsymbol{\zeta}}$, and $\bar{\boldsymbol{\xi}}$), it can be used as a valuable step in modeling spintronic systems with both complex anisotropy and multiple films. Specific test cases from Berreman's method were cross-checked with commercial software that use scattering matrix methods such as VASE by J. A. Woollam.

III. RESULTS AND DISCUSSION

A. Limits of quasimagnetostatic approximation

The dispersion relation of SMPs in MnF_2 , analytically found from Eq. (3), can be compared to poles of r_{ss} from Eq. (11). These poles are seen as peaks in the reflection amplitudes when plotted on a mesh of the real component

of the in-plane wave vector and angular frequency within the restrahlen band. Note that this assumes no k_y component, and does not contain information regarding propagation lengths as the imaginary component of k_x is set to zero. This comparison is seen in Fig. 3, with the quasimagnetostatic modes in red superposed on the color map showing the numerically derived values from the transfer method. The plots describe an air/MnF₂/air system. The axes are plotted in dimensionless units of reduced real components of the in-plane wave vector and reduced frequency. The resonant angular frequency ω_0 seen in Eq. (4) is used as a scale of normalization. The color maps show the absolute value squared of the reflection amplitudes for s -polarized light. As done with all the color maps in this work, the data are normalized to have values between 1 and 10 such that the logarithm seen in the figures varies between 0 and 1. It should be emphasised that throughout this work the term “reflectivity” will be used instead of the absolute value squared of the reflection amplitude. This quantity will be represented by the symbol \mathfrak{R} , distinguishing itself from the observable reflectivity R_{ss} . The quotation marks are used as reflectivity should be an experimental observable ranging between 0 and 1. As these dispersion curves show the same quantity for in-plane wave vectors unreachable via prism coupling, it is not equivalent to an observable reflectivity. The prism is required for coupling as the SMPs exist at wave vectors larger than that of air’s light line. Note that this is not true for some specific surface polaritons systems [37]. Figure 3 also shows the light line of a highly resistive Si prism. Momentum matching requirements can then only be achieved to the left of this line. The optical response of Si can be approximated by a Drude model such as [38]

$$\tilde{\epsilon} = \epsilon_{\text{Si}} - \frac{\omega_p^2}{\omega(\omega + i\Gamma)}, \quad (12)$$

where $\epsilon_{\text{Si}} = 11.66$ is the undoped permittivity, Γ is the scattering rate, and ω_p is the un-screened plasma frequency. If the carrier concentration density is assumed to be negligible, then ω_p goes to zero such that the silicon wafer can be approximated as nondispersive with $\epsilon = \epsilon_{\text{Si}}$. This silicon light line appears almost vertical. This is an artifact of the range of in-plane wave vectors being orders of magnitude greater than the restrahlen band of frequencies. Although thin MnF₂ films result in extremely large in-plane wave vectors [as seen in Fig. 3(a)], these highly confined modes are largely unreachable via means of prism coupling. In this work thicker films will be studied in which prism coupling into multiple modes can be achieved. As seen in Fig. 3(c), in the region in which coupling can be achieved (left of the silicon light line) the quasimagnetostatic approximation becomes less valid and the TMM should instead be employed.

B. Thin MnF₂ film in air

In this section we model attenuated total reflection measurements employing a high-index Si prism on top of an air gap spacer above the MnF₂ film. Distinct from the previous discussion in which $\epsilon = 1$ was assumed, the permittivity of MnF₂ is taken to be $\epsilon = 5.5$. This means a slab waveguide mode is supported in addition to the SMPs previously described. Figure 4(a) shows the dispersion of this waveguide

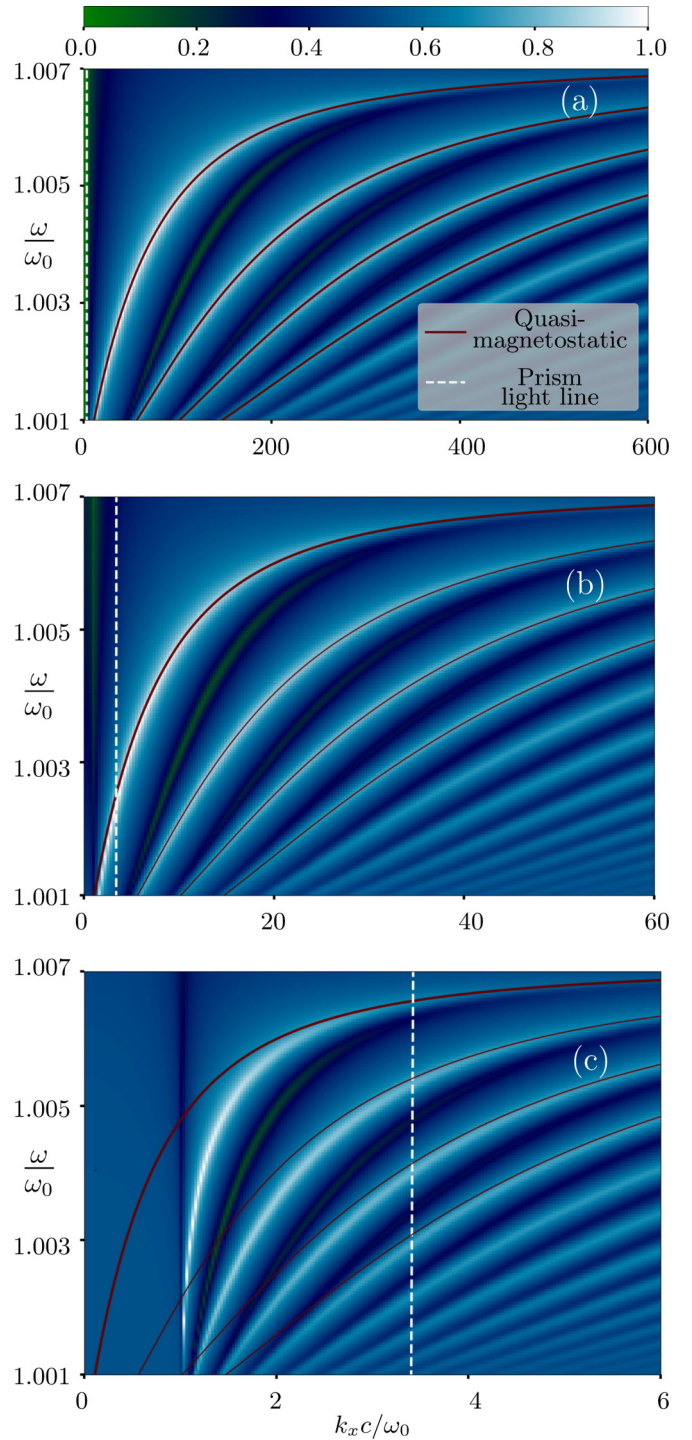


FIG. 3. Dispersion relations of the SMP modes supported by the air/MnF₂/air system, seen in Fig. 1. The analytically derived dispersion relation of the quasimagnetostatic modes of MnF₂ are shown by red curves. The color maps correspond to the normalized $\log_{10}(\mathfrak{R}_{ss})$, numerically calculated via the transfer method. The 3 graphs are calculated for varying MnF₂ film thicknesses (a) 5 μm , (b) 50 μm , and (c) 500 μm .

and the first 3 SMP modes for a 100 μm thin film of MnF₂ in air. It shows a supported waveguide mode with little dispersion at approximately $k_x = 1.3\omega_0/c$. This mode splits into the 0th-order SMP mode. The real and imaginary components

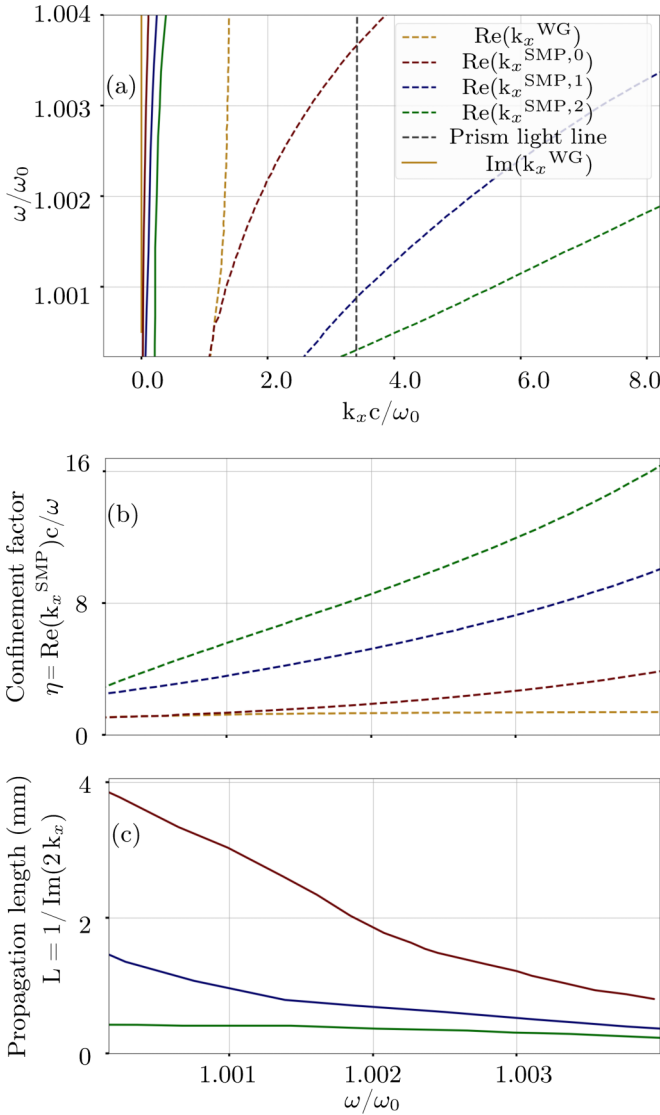


FIG. 4. (a) The SMP dispersion as a function of reduced in-plane wave vector and reduced angular frequency for a Si prism/air gap spacer/ $100 \mu\text{m}$ MnF_2 film/air system. The figure shows the dispersion of the waveguide mode (yellow), the first 3 SMP modes (red, blue, green), and prism light line (black), with the real components (full lines) and imaginary components (dashed lines). (b) The confinement factor $\eta = \text{Re}(k_x^{\text{SMP}})c/\omega$ and (c) the propagation length $L = 1/\text{Im}(2k_x^{\text{SMP}})$, of the waveguide and SMP modes in MnF_2 , as a function of reduced frequency.

of the in-plane wave vectors were calculated by the use of Muller's complex root finding algorithm [39]. For a discrete set of ω values, this algorithm was applied to determine the complex in-plane wave vectors k_x^{SMP} for the first few SMPs. It can be seen from Fig. 4(a) that the loss (seen in the imaginary component of in-plane wave vector) is negligible for the waveguide mode and grows with the index number of each SMP mode. Figure 4(b) shows the confinement factor $\eta = \text{Re}(k_x^{\text{SMP}})c/\omega$ as a function of reduced frequency. A confinement factor measures how compressed the transverse wavelength of the surface mode is as compared to the wavelength in air. Consistent with the imaginary components of the

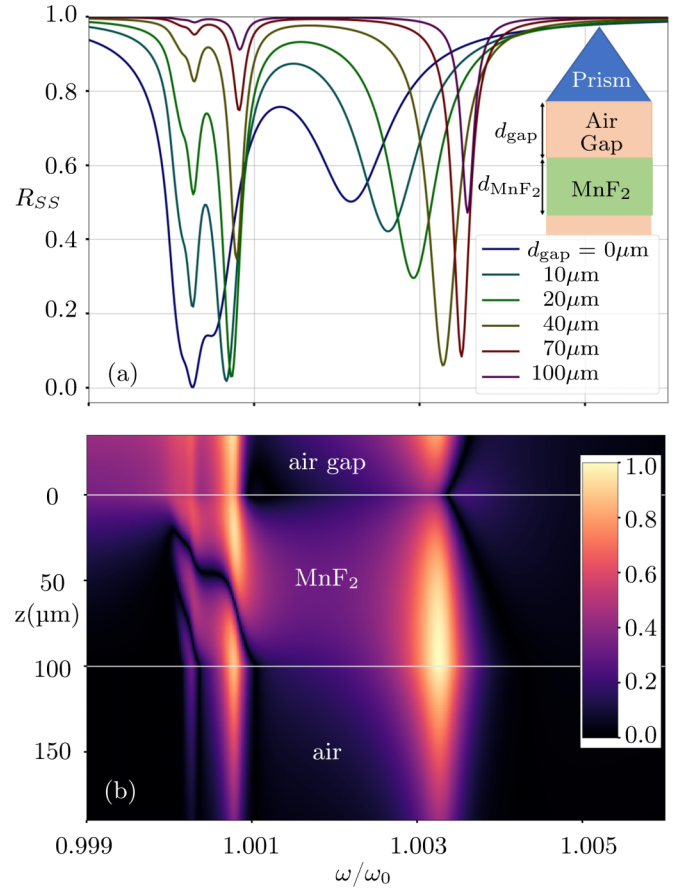


FIG. 5. (a) R_{SS} for various air gap thicknesses as seen in the legend for a prism/air gap spacer/ $100 \mu\text{m}$ MnF_2 /air system, as seen in the inset. (b) The y component of the electric field as a function of both reduced frequency and z distance, measured in μm , but with an air gap of $40 \mu\text{m}$. An incident angle of 80° was used in all cases. The color map shows the normalized logarithm of the absolute value of the y component of the electric field $\log_{10}(|E_y|)$.

SMPs in Fig. 4(a), the propagation length decreases with each mode index. Figure 4(c) shows the propagation length $L = 1/\text{Im}(2k_x^{\text{SMP}})$ in millimeters. The propagation length measures the transverse distance at which the polariton's intensity has reduced by $\exp(-1)$. Figure 4(b) and Fig. 4(c) show that with increasing frequency the mode confinement factors increase while the propagation lengths decrease. This trade-off between transverse confinement and propagation length is a characteristic feature of a surface polariton.

As previously mentioned, momentum matching is achieved in this work via the use of a high-index, resistive Si prism, with its relative permittivity approximated at 11.66. Figure 5(a) shows the reflectivity of s-polarized light for a Si prism/air gap spacer/ $100 \mu\text{m}$ MnF_2 film/air system. The incidence beam was set to be in the x - z plane (i.e., $k_y = 0$) with the polar angle set as $\theta_i = 80^\circ$ (from within the prism), where $k_x = (\omega/c) \sin(\theta_i \pi/180)$. It is observed that by increasing the air gap thickness, the resonances (seen as dips in the reflectivity) shift to higher frequencies. The air gap thickness which causes optimal coupling between the evanescent electric field (due to total internal reflection) and the SMP mode is known as the critical coupling length. This critical coupling length is

shown to be larger for lower order modes, with the 0th-order mode having a critical air gap of between 40 and 70 μm at a frequency of $1.0035\omega_0$. The critical coupling length for higher-order modes tends toward 0 μm as the losses associated with the prism become negligible compared to those intrinsic to the SMP's propagation. It therefore follows for experimental THz considerations that in order to gain control of and couple into a spin wave, a specific order mode should be chosen along with its corresponding critical coupling length. This follows as critical coupling is achieved when the losses back to the prism match the losses intrinsic to the SMP [40]. For air gaps smaller than 40 μm the losses back into the prism for the 0th-order mode dominate and the resonance broadens, weakens, and redshifts.

Figure 5(b) shows a color map of the absolute value of the y component of the electric field, $|E_y|$, as a function of reduced frequency and z distance in μm with an air gap of 40 μm . The incident angle was again set to $\theta_i = 80^\circ$. Three distinct enhancements can be seen in terms of frequency corresponding to the first 3 SMP resonances. The 0th-order mode enhancement, at $1.0032\omega_0$, shows a peak in field strength at the bottom interface. The 1st-order mode enhancement at $1.0008\omega_0$ has a minimum in field strength in the middle of the film and is maximum at either interface. Likewise, the weaker, 2nd-order SMP mode has two minima in the field strength within the film. In summary, the order of the mode corresponds to the number of minima in the field strength enhancement. This is analogous to the field profiles in slab waveguides and consequently these modes, supported only in the restrahlen bands of hyperbolic media, have been called subdiffraction guided waves [41]. The frequency slices in Fig. 5(b) show a generally asymmetric field profile. This is a consequence of the prism causing an asymmetry in the system.

C. Thin MnF₂ film with Si substrate

Antiferromagnetic semiconductors such as MnF₂ are most commonly fabricated via molecular-beam epitaxy (MBE) [42]. Lattice matching between a base material and the antiferromagnetic semiconductor results often in the use of silicon (001) as a substrate. In practice any measurements of the dispersion of SMPs on MnF₂ should also include this silicon (001) substrate. The previous system is now modified to include such a silicon substrate. Figure 6 shows, similarly to Fig. 3, a color map of the “reflectivity” \mathfrak{R}_{ss} as a function of reduced in-plane wave vector and frequency. Here the silicon was assumed highly resistive, such that a nondispersive relative permittivity of 11.66 could be used. The 3 white dashed lines in Fig. 6—I, II, and III—correspond to the light lines of air, MnF₂ (away from the restrahlen band), and Si, respectively. The modes with less dispersion seen to the left of Si's light line correspond to multiple slab waveguide modes arising from the asymmetric MnF₂/Si layer in air. Some of these modes are evanescent in the MnF₂ layer while others are propagating. It can be seen that some of these modes straddle both the air and MnF₂ light lines. To the right of these slab waveguide modes, multiple SMP modes can be seen in peaks of the “reflectivity.” The peaks resemble those seen without the substrate in Fig. 3, but are shifted to slightly

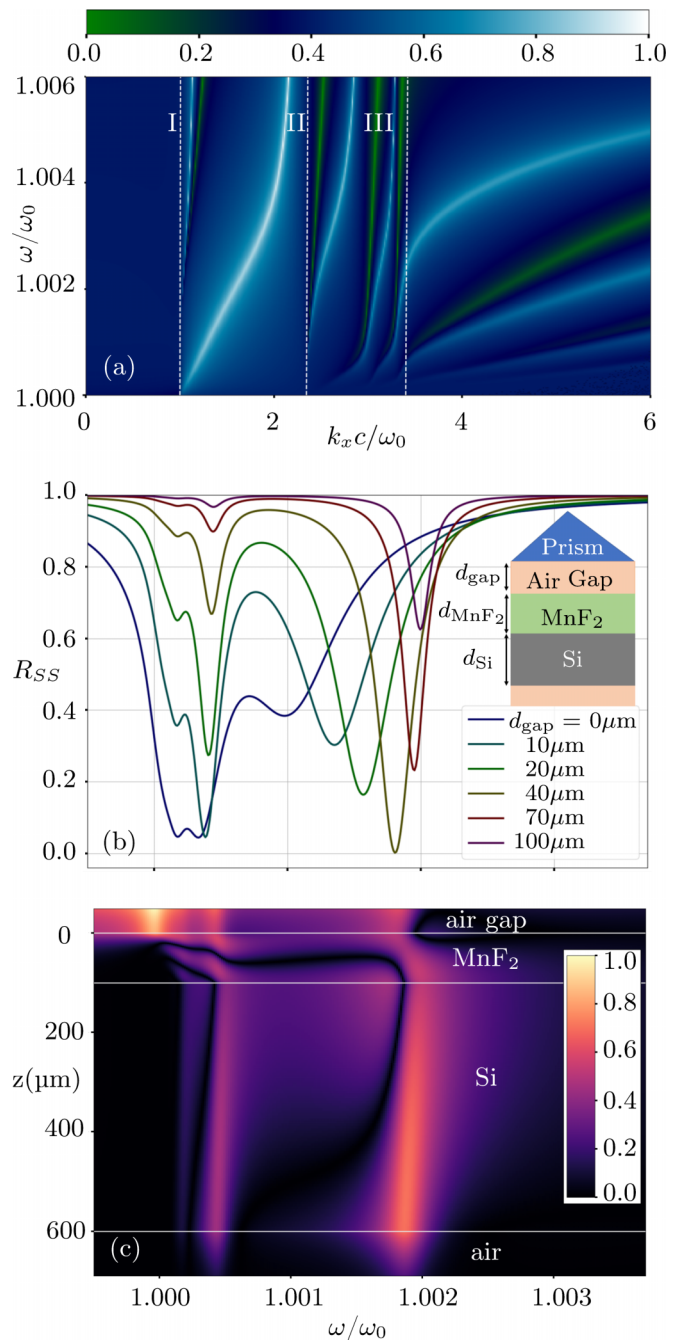


FIG. 6. (a) The “reflectivity” $\log_{10}(\mathfrak{R}_{ss})$ (as seen in the color map) of s -polarized light as a function of reduced real component of the in-plane wave vector and reduced angular frequency for an air/100 μm MnF₂/500 μm Si substrate/air system. (b) The reflectivity as a function of reduced angular frequency plotted for various air gap thicknesses as shown in the legends for a prism/air gap spacer/MnF₂/Si substrate/air system; see inset. (c) The y component of the electric field as a function of both reduced frequency and z distance, measured in μm , but where a fixed air gap of 40 μm was used. The color map shows the normalized logarithm of the absolute value of the y component of the electric field $\log_{10}(|E_y|)$. For both panels (b) and (c) an incident angle of 80° was used.

lower frequencies. It should be reminded that these types of color maps are only functions of the real component of the in-plane wave vector. The imaginary component has been set

to zero. This is the reason the slab waveguide mode appears brightest on the color map. If the imaginary component of the in-plane wave vector were increased, the higher loss modes would instead be most prominent on the color map.

As in the case in Fig. 5, a prism coupling experiment can be simulated. The polar angle was again set to 80° while a prism/air gap spacer/MnF₂/Si/air system was used with fixed layer thicknesses $d_{\text{MnF}_2} = 100 \mu\text{m}$ and $d_{\text{Si}} = 500 \mu\text{m}$. The system is depicted in the inset of Fig. 6(b). Figure 6(b) also shows the reflectivity of *s*-polarized light as a function of reduced frequency for various air gap thicknesses as shown in the legend. The criteria for the critical coupling length of each mode is altered by the Si wafer. Maximum coupling is achieved when the intrinsic losses present in each SMP equal the losses back to the prism as well as those through the MnF₂ layer and into the Si wafer. This is seen by comparing Fig. 5(a) and Fig. 6(b) as the addition of the Si wafer causes a slight decrease in critical coupling length. Figure 6(b) shows that the critical coupling length of the 0th-order mode occurs at a lower thickness than without the Si layer, with $d_{\text{gap}} = 40 \mu\text{m}$. The higher-order modes are also altered in that there is no longer a thickness which results in full extinction of the reflectivity. The main consequence of the addition of a Si wafer is a collective redshift of the modes toward ω_0 . This redshift could be problematic when considering experimental designs in the THz. As the already narrow bandwidth within which the SMPs becomes even smaller, resolving specific SMP modes would become harder.

Figure 6(c) shows $|E_y|$ as a function of both reduced frequency and *z* distance measured in μm . The color map is on a logarithmic scale. Figure 6(c) shows three main resonances occurring at frequencies $\omega/\omega_0 = 1.0019, 1.0003, \text{ and } 1.0002$. The modes again show the features that the number of field minimums in the MnF₂ layer equal the mode index and that the modes lie to the right of MnF₂'s light line warranting the name subdiffractive waveguide modes. The effect of the Si wafer is that the evanescent fields inside the MnF₂ become propagating in the wafer and leak energy out of the MnF₂ layer.

D. Thin MnF₂ film with SiO₂ substrate

The use of a high-index Si wafer results in a leakage of energy from within the MnF₂ into the substrate. A more optimal choice of substrate (in terms of field enhancement) would be SiO₂, as it has a lower index and suitable lattice parameters. An additional issue with the Si wafer used in Fig. 6 is that because it is many times thicker than the SMP-supporting MnF₂ layer, the energy from the prism is more likely to leak into the substrate. For these reasons Fig. 7 models an identical system except the $500 \mu\text{m}$ Si wafer is replaced by a $275 \mu\text{m}$ SiO₂ substrate. For simplicity, the SiO₂ is assumed to be nondispersive and characterized by $\text{Re}(\epsilon) = 3.9$ and $\text{Re}(\mu) = 1.0$ [43]. Figure 7(a) shows a color map of the “reflectivity” of a Si prism/air gap spacer/ $100 \mu\text{m}$ MnF₂ film/ $257 \mu\text{m}$ SiO₂ wafer/air system as a function of the real component of reduced in-plane wave vector and reduced angular frequency. The 3 dashed lines in Fig. 7 labeled I, II, and III correspond to the light lines of air, the SiO₂ substrate, and Si prism, respectively. The dispersion curves are similar to those seen

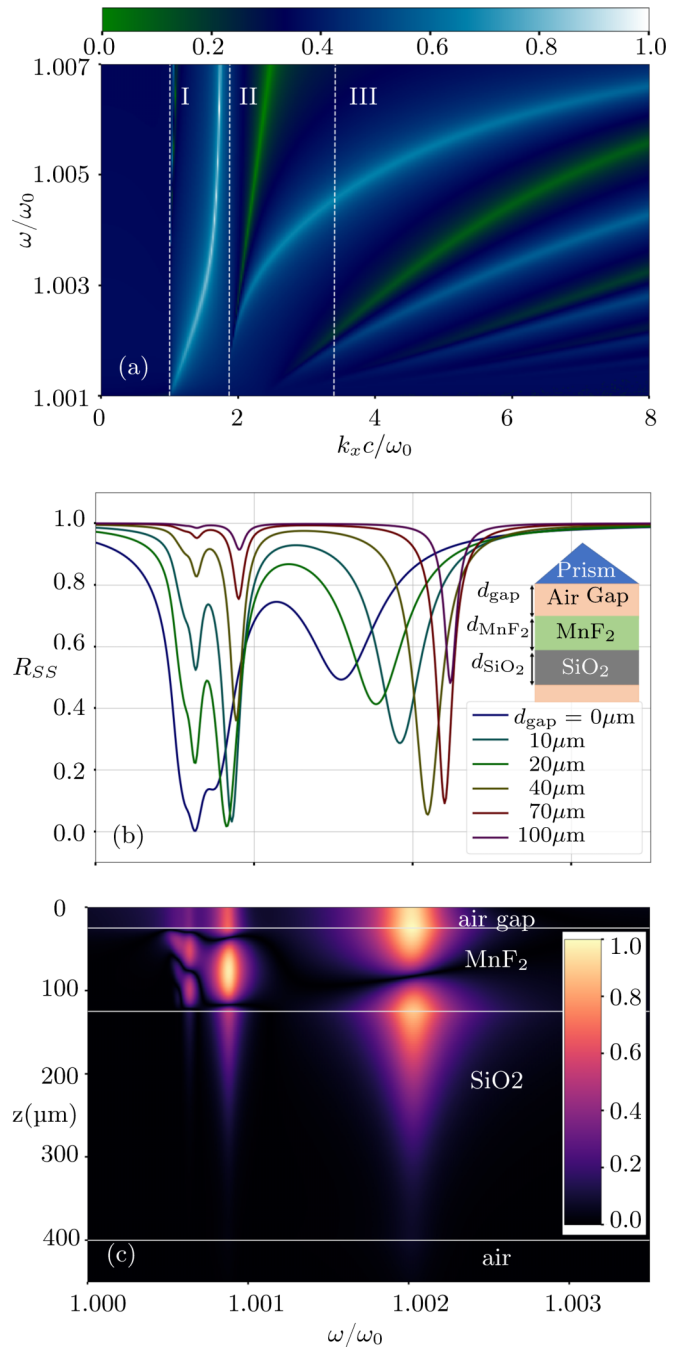


FIG. 7. (a) The “reflectivity” $\log_{10}(\mathcal{R}_{ss})$ (as seen in the color map) of *s*-polarized light as a function of reduced real component of the in-plane wave vector and reduced angular frequency for an air/ $100 \mu\text{m}$ MnF₂/ $275 \mu\text{m}$ SiO₂ substrate/air system. (b) The reflectivity as a function of reduced angular frequency plotted for various air gap thicknesses as shown in the legends for a prism/air gap spacer/MnF₂/SiO₂ substrate/air system; see inset. (c) The *y* component of the electric field as a function of both reduced frequency and *z* distance, measured in μm , but where a fixed air gap of $40 \mu\text{m}$ was used. The color map shows the normalized logarithm of the absolute value of the *y* component of the electric field $\log_{10}(|E_y|)$. For both panels (b) and (c) an incident angle of 80° was used.

in Fig. 6 except there are fewer slab waveguide modes due to the decreased thickness of the substrate. Note that in these sections, the term substrate refers to the wafer on which films

are grown and not the semi-infinite layer at the bottom of the system. In all the simulations in this work the semi-infinite layer below the stack is always assumed to be air. The SMP modes are shifted to higher wave vectors than seen in Fig. 5(a) when no substrate is used, but lower than in Fig. 6(a) when a Si wafer is employed. It should be noted that although the prism's light line is present, the dispersion plots present in this work are for the modes before any coupling mechanism is used. Figure 7(b) shows the reflectivity of *s*-polarized light as a function of reduced angular frequency for the same system. It strongly resembles Fig. 6(b), except it is slightly less redshifted than when no substrate is used. One explanation for why higher permittivity substrates cause redshifting in these SMP resonances could be seen from basic SPP theory. For a single interface between a dielectric and a metal with relative permittivities ϵ_1 and ϵ_2 , respectively, the SPP resonance ω_{SPP} occurs at

$$\omega_{\text{SPP}} = \frac{\omega_p}{\sqrt{\epsilon_1 + \epsilon_2}}, \quad (13)$$

where ω_p is the plasma frequency of the metal. Although this equation is derived using a Drude model for ϵ , while μ in the MnF_2 films takes a Lorentzian form, the trend of decreasing resonant frequency for substrates with increasing dielectric constants is observed. Figure 7(c) shows $|E_y|$ as a function of both reduced angular frequency and distance in the *z* direction as measured in μm for the system with a SiO_2 substrate. It shows again 3 main resonances occurring at approximately $\omega/\omega_0 = 1.002$, 1.0008, and 1.0006. The plot displays much faster spatial decay into the substrate than when compared with 6(c). An additional notable feature is that the number of zero points along the field profile corresponds to 1 more than its mode index. The field profiles also look relatively more symmetric in intensity than when compared with the previous systems. This artifact could be due to the layers either side of the MnF_2 layer, air gap/Si and SiO_2 /air, having more coupling symmetry than with the previous systems. SiO_2 may then present itself as a better choice of growth wafer when compared to Si as the system appears more symmetric and would require less extreme spectral resolution to resolve different SMP orders.

E. Ultrathin MnF_2 films

So far in this work attenuated total reflection (ATR) measurements have been simulated for 100 μm thick MnF_2 films. This thickness has been used as it allows multimode coupling to be observed. Due to current limitations in MBE methods such thicknesses are highly unfeasible. More realistic growth thicknesses from MBE range from 50 to 500 nm. To simulate a more realistic ATR experiment (in terms of current MBE limitations) a MnF_2 film thickness of 100 nm was instead used. Figure 8 shows results for a Si prism/air gap spacer/100 nm MnF_2 layer/275 μm /air system. Figure 8(a) shows a “reflectivity” map as a function of real component of the reduced in-plane wave vector and reduced angular frequency. It can be seen that the frequency range plotted has been reduced to a very thin span centered on ω_0 . This is an artifact of the SMP modes becoming increasingly confined as the film thickness is decreased. Consequently, the only mode observable within

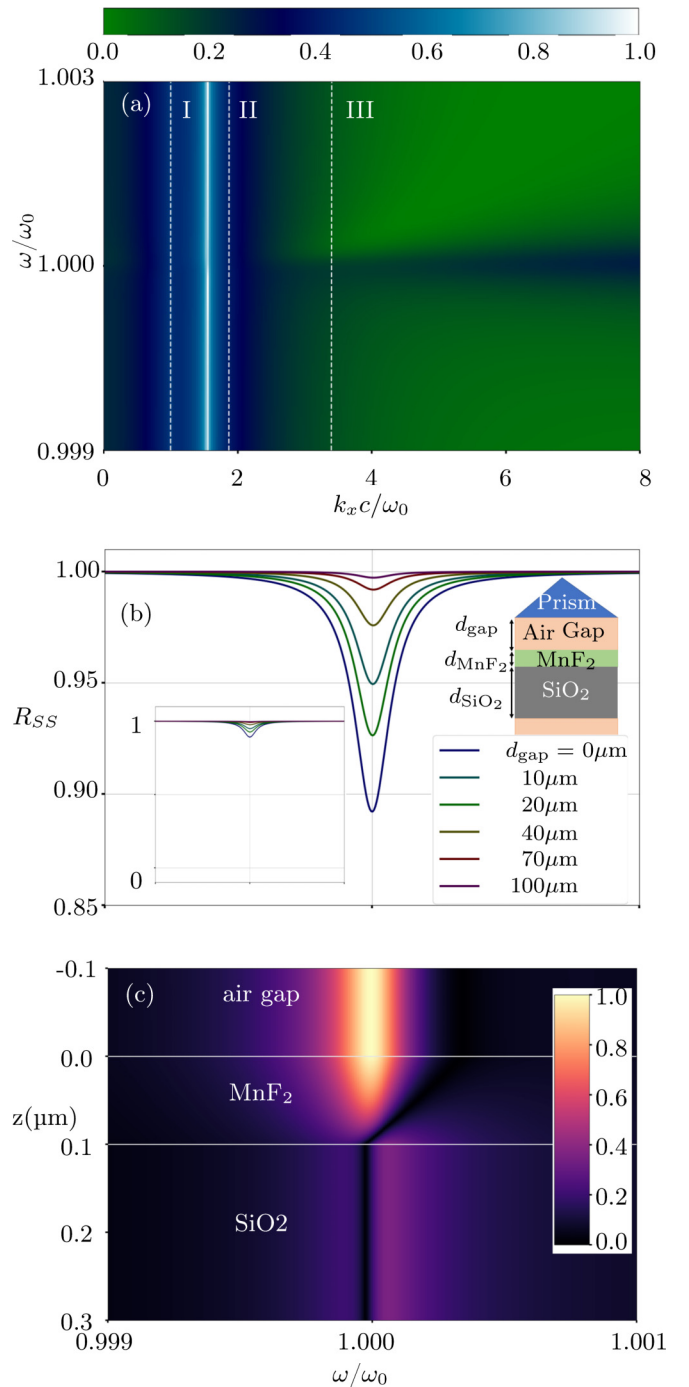


FIG. 8. (a) The “reflectivity” $\log_{10}(\mathfrak{R}_{ss})$ (as seen in the color map) of *s*-polarized light as a function of reduced real component of the in-plane wave vector and reduced angular frequency for an air/100 nm MnF_2 /275 μm SiO_2 substrate/air system. (b) The reflectivity as a function of reduced angular frequency plotted for various air gap thicknesses as shown in the legends for a prism/air gap spacer/ MnF_2 / SiO_2 substrate/air system; see right inset. Reflectivity is plotted on full scale; see left inset. (c) The *y* component of the electric field as a function of both reduced frequency and *z* distance, measured in μm , but where a fixed air gap of 5 μm was used. The color map shows the normalized logarithm of the absolute value of the *y* component of the electric field $\log_{10}(|E_y|)$. For both panels (b) and (c) an incident angle of 80° was used.

the Si prism's light line is the 0th-order mode. The position of this mode is also shifted toward the resonance at ω_0 . The mode appears very weak on account of the MnF₂ layer only being 1/10 000th of the resonant wavelength. The weak response of this resonance is demonstrated in Fig. 8(b) where the reflectivity is plotted as a function of reduced frequency for various air gap thicknesses with again an incident angle of 80°. The weakness of the response is seen in the inset in which the reflectivity is plotted on the full reflectivity scale instead of starting from 0.85. The legend shows that the critical coupling efficiency occurs for $d_{\text{air gap}} = 0 \mu\text{m}$. This is likely due to the mode having high losses, such that even if energy is coupled back into the prism, by reducing the air gap, the intrinsic losses in the mode are still higher. This is consistent with the fact that the permeability shows a peak in its imaginary component at ω_0 , as seen in Fig. 2. The absolute value of the y component of the electric field is shown on a color plot as a function of reduced angular frequency and distance in the z direction as measured in μm in Fig. 8(c). The plot shows one resonance [like in Fig. 8(b)] at ω_0 . The mode decays quickly with increasing z distance into the MnF₂ layer. In the SiO₂ layer, a field enhancement can be seen on either side of the resonance at ω_0 . The field, however, is extinct at ω_0 due to the absorption within the MnF₂ layer at this frequency. The weakness and extremely small linewidth of this resonance means a terahertz system must have both a large signal-to-noise ratio and a very high spectral resolution. For most THz sources this high spectral resolution can only be achieved through the use of a long delay line.

F. Arbitrary rotation of MnF₂ easy axis

A benefit of the 4×4 transfer method is that it can accommodate materials with full bianisotropic optical constants seen in the dimensionless optical matrix

$$\bar{\mathbf{M}} = \begin{bmatrix} \bar{\boldsymbol{\epsilon}} & \bar{\boldsymbol{\xi}} \\ \bar{\boldsymbol{\zeta}} & \bar{\boldsymbol{\mu}} \end{bmatrix}, \quad (14)$$

where $\bar{\boldsymbol{\xi}}$ and $\bar{\boldsymbol{\zeta}}$ are the bianisotropic, cross-polarization terms. In this work these terms have been set to zero while the tensor $\bar{\boldsymbol{\epsilon}}$ has been modeled as isotropic for the MnF₂ crystal. So far in this paper it has been assumed that the crystal axis of the MnF₂ film is in the same reference frame as the laboratory frame. Through Euler rotations to the crystal axis, the easy axis (axis of anisotropy) can be rotated to any angle such the laboratory frame tensor $\bar{\boldsymbol{\mu}}_{\text{la}}$ is given by

$$\bar{\boldsymbol{\mu}}_{\text{la}} = \bar{\mathbf{A}}_{\text{rot}}(\phi_r, \theta_r, \psi_r) \bar{\boldsymbol{\mu}}_{\text{ca}} \bar{\mathbf{A}}_{\text{rot}}(\phi_r, \theta_r, \psi_r)^{-1}, \quad (15)$$

where $\bar{\boldsymbol{\mu}}_{\text{ca}}$ is the permeability tensor in the crystal's reference frame and $\bar{\mathbf{A}}_{\text{rot}}(\phi_r, \theta_r, \psi_r)$ is the rotation matrix. The angles ϕ_r , θ_r , and ψ_r are defined as rotations about the crystal's z axis, the crystal's new y axis, and the new z axis, respectively.

This work will now simulate rotating the crystal axis of MnF₂ by various angles of θ_r turning the easy axis toward the laboratory's y axis (as seen in Fig. 1). The effect of such rotations is seen in Fig. 9 in which the real part of the 3 diagonal components of $\boldsymbol{\mu}$ is shown as a function of reduced frequency. Figure 9 presents the dependence of $\text{Re}[\boldsymbol{\mu}(\omega)]$ vs angular frequency ω for rotation angles $\theta_r = 0^\circ$, 40° , and 90° when $\phi_r = 90^\circ$. Figure 9(a) shows a region shaded in brown

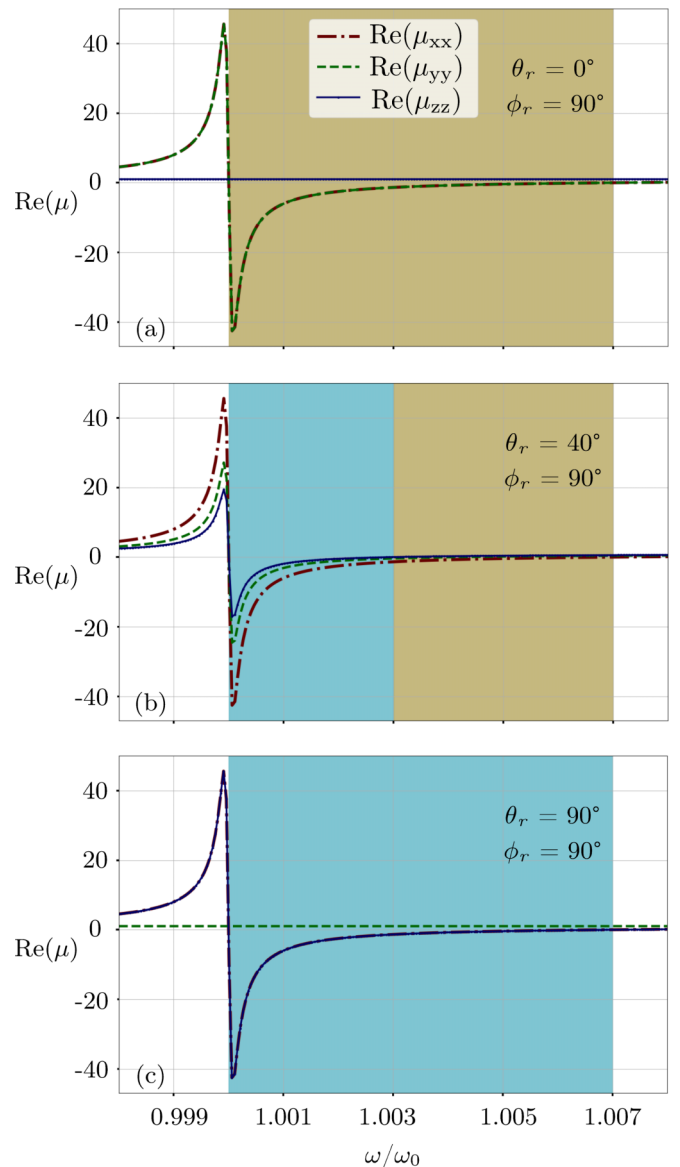


FIG. 9. Real components of the diagonal elements of the permeability tensor of MnF₂ as seen in the legend. Regions within the restrahlen band shaded brown correspond to $\text{Re}(\mu_{xx})$ being negative and $\text{Re}(\mu_{yy})$ being positive. Regions shaded blue correspond to both $\text{Re}(\mu_{xx})$ and μ_{zz} being negative. (a) Euler angles set to $\phi_r = 90^\circ$ and $\theta_r = 0^\circ$. (b) Euler angles set to $\phi_r = 90^\circ$ and $\theta_r = 40^\circ$. (c) Euler angles set to $\phi_r = 90^\circ$ and $\theta_r = 90^\circ$.

representing the restrahlen band of the in-plane component of the permeability tensor while the out-of-plane component is constantly equal to 1. For s -polarized light this results in the type II hyperbolic dispersion which enables the SMP modes seen in this work. With an angle $\theta_r = 40^\circ$, Fig. 9(b) shows the restrahlen band partitioned into two sections, shaded blue and brown. The blue section represents the frequency region for which both $\text{Re}(\mu_{xx})$ and $\text{Re}(\mu_{zz})$ are negative, while the brown region still represents a type II hyperbolic dispersion. Figure 9(c) shows the permeability when $\theta_r = 90^\circ$. Here the easy axis is in the y direction such that both the x and z terms are equal. The dispersion is then isotropic as labeled by the blue shaded region.

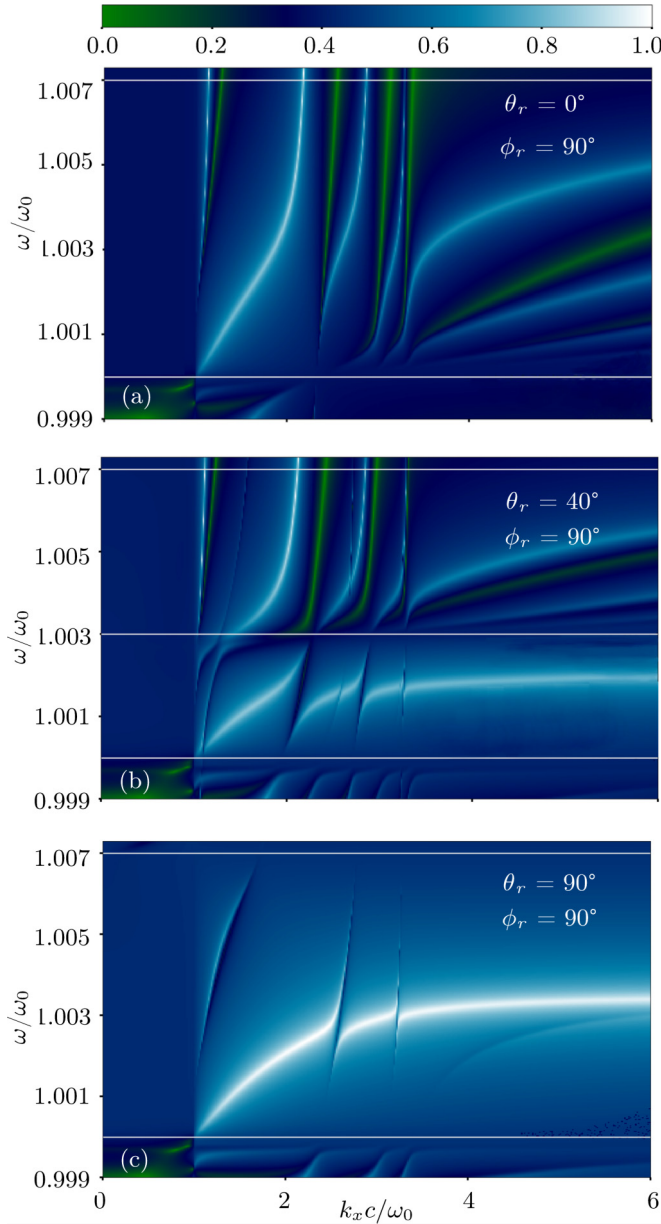


FIG. 10. “Reflectivity” $\log_{10}(\mathfrak{R}_{ss})$ (as seen in the color map) plots of s -polarized light as a function of reduced real component of the in-plane wave vector and reduced angular frequency of an air/ $100\ \mu\text{m}$ MnF₂/ $500\ \mu\text{m}$ Si substrate/air system. Restrahlen band is indicated by top and bottom horizontal lines. (a) Euler angles were set to $\phi_r = 90^\circ$ and $\theta_r = 0^\circ$. (b) Euler angles were set to $\phi_r = 90^\circ$ and $\theta_r = 40^\circ$; the middle horizontal line corresponds to a change in sign of μ_{zz} . (c) Euler angles were set to $\phi_r = 90^\circ$ and $\theta_r = 90^\circ$.

The dispersion is then plotted for these three cases of rotated crystal axis, as seen in Fig. 10. For these simulations concerning crystal axis rotations, an air/ $100\ \mu\text{m}$ MnF₂ film/ $500\ \mu\text{m}$ Si substrate/air system is used. No prism is employed in this section as the dispersion is of interest, as opposed to any coupling mechanism. Silicon is used as a wafer instead of SiO₂ as its higher index supports more slab waveguide modes, offering a more complex dispersion relation. Figure 10(a) is identical to Fig. 6(a) except a larger frequency range is used such that the restrahlen band can be

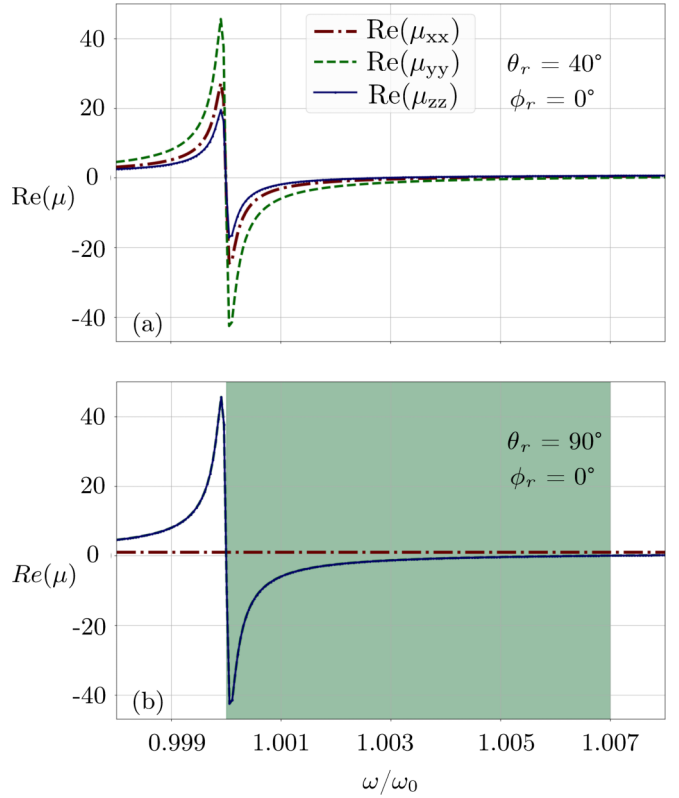


FIG. 11. Real components of the diagonal elements of the permeability tensor of MnF₂ as seen in the legend. (a) Euler angles were set to $\phi_r = 0^\circ$ and $\theta_r = 40^\circ$. (b) Euler angles were set to $\phi_r = 90^\circ$ and $\theta_r = 40^\circ$. The frequency region shaded green corresponds to $\text{Re}(\mu_{xx})$ and $\text{Re}(\mu_{zz})$ both being negative.

seen bounded by the two horizontal white lines. Figure 10(b) shows the dispersion for $\theta_r = 40^\circ$ and can be separated into two regions of frequency exhibiting different dispersion. From ω_0 to $1.003\omega_0$ both $\text{Re}(\mu_{xx})$ and $\text{Re}(\mu_{zz})$ are negative. The dispersion consequentially behaves as a normal SMP, supporting one single mode (this is typical for a film in an asymmetric system). In the frequency region from $1.003\omega_0$ to $1.007\omega_0$, $\text{Re}(\mu_{zz})$ becomes positive so that subdiffracted waveguide type SMPs can again be supported. This is a result of the permeability tensor again having the form of a type II hyperbolic material. Figure 10(c) shows the dispersion for $\theta_r = 90^\circ$. Here the permeability is isotropic as both μ_{xx} and μ_{zz} follow the Lorentzian shape predicted by Eq. (4). It can be seen that now the full restrahlen band supports only normal SMPs/SPPs. A fainter mode is seen below the dominant one. These two modes correspond to the long and short range modes seen in SPP or SMP supporting films. The lower mode is much weaker as the system is not symmetric. The plot also shows anti-level-crossings where the slab waveguide modes intersect the main SMP mode. These observed anti-level-crossings provide exciting research prospects for magnon-photon coupling, a topic that has recently sparked interest in the literature [44].

Figures 11 and 12 outline a similar simulation to the one seen in Figs. 9 and 10 except now the Euler angle ϕ_r is set to 0° . The consequence of this is that as θ_r is again rotated

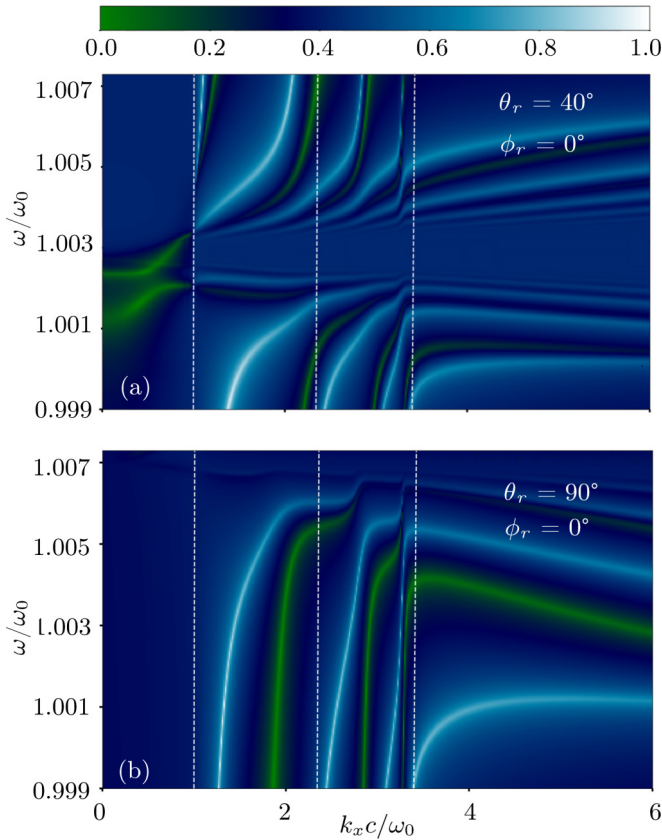


FIG. 12. “Reflectivity” $\log_{10}(\mathfrak{R}_{rs})$ (as seen in the color map) plots of s -polarized light as a function of reduced real component of the in-plane wave vector and reduced angular frequency of an air/100 μm MnF₂/500 μm Si substrate/air system. (a) Euler angles were set to $\phi_r = 0^\circ$ and $\theta_r = 40^\circ$. (b) Euler angles were set to $\phi_r = 0^\circ$ and $\theta_r = 90^\circ$.

through 90° , the easy axis is pivoted from being in the z direction to being in the x direction. In terms of dispersion, the permeability within the restrahlen band goes from being a type II hyperbolic material [with $\text{Re}(\mu_{xx}) < 0$ and $\text{Re}(\mu_{zz}) > 0$] to that of a type I hyperbolic material [with $\text{Re}(\mu_{xx}) > 0$ and $\text{Re}(\mu_{zz}) < 0$]. Figures 11(a) and 11(b) show the real components of the 3 diagonal elements of the MnF₂ permeability tensor. In Fig. 11(a) the Euler angles are set to $\phi_r = 0^\circ$ and $\theta_r = 40^\circ$. Here the response is anisotropic with both terms $\text{Re}(\mu_{xx})$ and $\text{Re}(\mu_{zz})$ being mainly negative but distinct. The restrahlen band is now less defined as the different tensorial elements of the permeability are negative at different frequencies. In Fig. 11(b) the rotation angles are set to $\phi_r = 0^\circ$ and $\theta_r = 90^\circ$. The restrahlen band is now well defined and shaded green with $\text{Re}(\mu_{zz})$ being negative between ω_0 and $1.007\omega_0$. The material then behaves as a type I hyperbolic material.

Figure 12 presents the SMP dispersion as functions of the real part of reduced in-plane wave vector and reduced angular frequency for the two cases seen in Fig. 11. For $\phi_r = 0^\circ$ and $\theta_r = 40^\circ$, as seen in Fig. 12(a), the SMP and the slab waveguide modes appear to be supported only outside a gap centered around $1.003\omega_0$. An interesting feature of the plot is that some of the slab waveguide modes appear to continuously transform into SMP modes, having less dispersive waveguide behavior

at low wave vectors and highly dispersive SMP behavior at higher wave vectors. A possible cause of the gap in which no modes exist is that it corresponds to a frequency region in which both $\text{Re}(\mu_{xx})$ and $\text{Re}(\mu_{zz})$ have magnitudes less than 1.

Figure 12(b) shows another dispersion plot but for both $\phi_r = 0^\circ$ and $\theta_r = 90^\circ$. With this crystal orientation, the region in which no modes can exist is now gone. For smaller wave vectors the modes appear to behave as waveguide modes. For large wave vectors the modes appear to become more dispersive, with many having a negative slope. This negative slope corresponds to a negative group velocity. Since these modes would then have a negative group velocity and a positive phase velocity, they would exhibit negative refraction [45]. Such refraction arises from the permeability’s type I hyperbolic form, also called its indefinite permeability [46]. In order to gain control and couple into SMPs, it is necessary to consider the structure’s more exotic features including anti-level-crossings and negative refraction.

G. Discussion

The flexibility of Berreman’s 4×4 TMM enables the study of the various types of SMPs supported by MnF₂ thin films. ATR and field enhancement simulations have been performed for systems with varying substrate materials and MnF₂ thicknesses. It was shown that SiO₂ is a more suitable substrate candidate than silicon as there is less energy leakage with the SiO₂ substrate. Moreover, when coupling into thinner MnF₂ films, THz systems must have both very high spectral resolution and signal-to-noise ratio. Varying the crystal axis of the MnF₂ layer showed that the dispersion can be tuned to support subdiffracted guided, normal SMPs and negative refractive SMPs when the permeability tensor has type II hyperbolic, isotropic and type I hyperbolic form, respectively.

The SMPs supported by MnF₂ have previously been studied both analytically in the magnetostatic limit for extremely thin films and through ATR simulations on semi-infinite crystals [47]. The current work explored Berreman’s TMM in order to rigorously investigate prism coupling into thicker (but still regarded optically thin at THz frequencies) films, for which the magnetostatic approximation is less accurate. Exploring this less studied domain allows the investigation of coupling into the multiple branches of the supported subdiffractive modes simultaneously for a constant angle of incidence. Although Berreman’s 4×4 matrix method has been previously used to study SPhP and heterojunction systems, it has not yet been applied to SMP systems in the THz domain [48,49]. Future studies can be envisaged to rectify certain simplifications made here. For example, the incident beam was assumed to be a plane wave, having a single angle of incidence. In practice, terahertz sources will have a finite angular beam spread, owing to the finite size of the radiating plasma created in the setup [50]. Other approximations made include the nondispersive modeling of the highly resistive Si prism, the various substrates, and that of air. In practice, there can be residual impurities in the MnF₂ film and the Si substrate, giving rise to an additional Drude behavior in the semiconductors, as well as water vapor in air causing absorption. An additional limitation of this approach is that the TMM used is not numerically stable for systems with thick films and

highly evanescent fields. Although this limit was not reached in this work, future studies on thicker films should implement the more stable scattering matrix formalism. This work offers insights into what to expect from future time-domain THz transmission spectroscopy or THz emission spectroscopy on more realistic SMP-supporting systems [1]. This should aid the development for future applications in fields including spintronics and subdiffractive optics.

IV. CONCLUSION

This work has explored the various types of SMPs supported by MnF_2 thin films with thicknesses for which the magnetostatic approximation is no longer valid. The effects of various alterations were investigated for relevant experimental configurations. The refractive index of the substrate was demonstrated to strongly affect the amount of energy leakage away from the SMP. Although thicker MnF_2 films enable interesting multimode coupling, current MBE limitations make only single-mode coupling achievable through ATR coupling. The reflectivity dip for such a system would be very narrow and weak, requiring a THz system with both high resolution

and sensitivity. Additionally, rotating the crystal axis of the MnF_2 film revealed a rich environment of modes, including multiply branched, negative refractive, and normal (isotropic) SMPs. Notable anti-level-crossings were also shown to exist between slab waveguide and subdiffractive SMP modes in the MnF_2 layer. Such features are rarely supported in equivalent SPP thin-film systems. Moreover, the speed and flexibility of Berreman's 4×4 TMM make it a valuable tool for modeling such complex systems. These methods could be integral for applications in spintronics and subdiffractive optics.

ACKNOWLEDGMENTS

N.H. acknowledges financial support from the NTNU-Nano fund. The authors also are grateful for partial funding by EEA Grant No. EMP-CZ-MOP-2-013. I.S. acknowledges partial support by the French National Research Agency (Grant No. ANR-15-CHIN-0003) and Sigma2 — the National Infrastructure for High-Performance Computing and Data Storage in Norway for the allocation of computer time. N.H. acknowledges useful discussions with Kamil Postava, Roland Richter, Mathias Hartl, Pierre Koleják, and Martin Mičica.

-
- [1] K. Grishunin, T. Huisman, G. Li, E. Mishina, T. Rasing, A. V. Kimel, K. Zhang, Z. Jin, S. Cao, W. Ren, G.-H. Ma, and R. V. Mikhaylovskiy, *ACS Photonics* **5**, 1375 (2018).
- [2] I. Žutić, F. Jaroslav, and S. D. Sarma, *Rev. Mod. Phys.* **76**, 323 (2004).
- [3] A. V. Chumak, V. I. Vasyuchka, A. A. Serga, and B. Hillebrands, *Nat. Phys.* **11**, 453 (2015).
- [4] D. N. Basov, M. M. Fogler, and F. J. García de Abajo, *Science* **354**, 6309 (2016).
- [5] D. Farmer, P. Avouris, Y. Li, T. Heinz, and S.-J. Han, *ACS Photonics* **3**, 553 (2016).
- [6] D. Rodrigo, O. Limaj, D. Janner, D. Etezadi, F. J. García de Abajo, V. Pruneri, and H. Altug, *Science* **349**, 165 (2015).
- [7] A. Poddubny, I. Iorsh, P. Belov, and Y. Kivshar, *Nat. Photonics* **7**, 948 (2013).
- [8] S. Dai, Q. Ma, T. Andersen, A. McLeod, Z. Fei, M. Liu, M. Wagner, K. Watanabe, T. Taniguchi, M. Thiemens, F. Keilmann, P. Jarillo-Herrero, M. Fogler, and D. Basov, *Nat. Commun.* **6**, 6963 (2015).
- [9] P. Li, M. Lewin, A. V. Kretinin, J. D. Caldwell, K. S. Novoselov, T. Taniguchi, K. Watanabe, F. Gaussmann, and T. Taubner, *Nat. Commun.* **6**, 7507 (2015).
- [10] S. Y. Buhmann and S. Scheel, *Phys. Rev. Lett.* **102**, 140404 (2009).
- [11] D. L. Mills and E. Burstein, *Rep. Prog. Phys.* **37**, 817 (1974).
- [12] M. I. Kaganov, N. B. Pustyl'nik, and T. I. Shalaeva, *Phys. Usp.* **40**, 181 (1997).
- [13] T. Yen, W. Padilla, N. Fang, and D. Vier, *Science* **303**, 1494 (2004).
- [14] W. Cai and V. Shalaev, *Optical Metamaterials* (Springer, New York, 2010).
- [15] K. W. Blazey, K. A. Müller, M. Ondris, and H. Rohrer, *Phys. Rev. Lett.* **24**, 105 (1970).
- [16] M. R. F. Jensen, S. A. Feiven, T. J. Parker, and R. E. Camley, *Phys. Rev. B* **55**, 2745 (1997).
- [17] J. P. Kotthaus and V. Jaccarino, *Phys. Rev. Lett.* **28**, 1649 (1972).
- [18] S. Bhatti, R. Sbiaa, A. Hirohata, H. Ohno, S. Fukami, and S. Piramanayagam, *Mater. Today* **20**, 530 (2017).
- [19] R. Macêdo, *Tunable Hyperbolic Media: Magnon-Polaritons in Canted Antiferromagnets* (Academic Press, 2017), pp. 91–155.
- [20] R. Macêdo and R. E. Camley, *Phys. Rev. B* **99**, 014437 (2019).
- [21] J. Sloan, N. Rivera, J. D. Joannopoulos, I. Kaminer, and M. Soljačić, *Phys. Rev. B* **100**, 235453 (2019).
- [22] A. Huber, N. Ocelic, D. Kazantsev, and R. Hillenbrand, *Appl. Phys. Lett.* **87**, 081103 (2005).
- [23] H. J. Falge and A. Otto, *Phys. Status Solidi B* **56**, 523 (1973).
- [24] S. Dai, Q. Ma, M. K. Liu, T. Andersen, Z. Fei, M. D. Goldflam, M. Wagner, K. Watanabe, T. Taniguchi, and M. Thiemens, *Nat. Nanotechnol.* **10**, 682 (2015).
- [25] P. Yeh, *Surf. Sci.* **96**, 41 (1980).
- [26] D. W. Berreman, *J. Opt. Soc. Am.* **62**, 502 (1972).
- [27] L. R. Walker, *Phys. Rev.* **105**, 390 (1957).
- [28] D. Stancil and A. Prabhakar, *Spin Waves* (Springer, New York, 2009).
- [29] S. A. Maier, *Plasmonics: Fundamentals and Applications* (Springer, New York, 2007).
- [30] C. Kittel, *Phys. Rev.* **82**, 565 (1951).
- [31] B. Lüthi, D. L. Mills, and R. E. Camley, *Phys. Rev. B* **28**, 1475 (1983).
- [32] T. Dumelow and M. C. Oliveros, *Phys. Rev. B* **55**, 994 (1997).
- [33] M. Schubert, *Phys. Rev. B* **53**, 4265 (1996).
- [34] F. Abelès, *Ann. Phys.* **12**, 596 (1950).
- [35] H. Wöhler, G. Haas, M. Fritsch, and D. A. Mlynski, *J. Opt. Soc. Am. A* **5**, 1554 (1988).

- [36] W. Xu, L. T. Wood, and T. D. Golding, *Phys. Rev. B* **61**, 1740 (2000).
- [37] T. Dumelow, *J. Phys.: Condens. Matter* **10**, 7809 (1998).
- [38] S. Nashima, O. Morikawa, K. Takata, and M. Hangyo, *Appl. Phys. Lett.* **79**, 3923 (2001).
- [39] D. E. Muller, *Mathematical Tables and Other Aids to Computation* **10**, 208 (1956).
- [40] B. Neuner III, D. Korobkin, C. Fietz, D. Carole, G. Ferro, and G. Shvets, *Opt. Lett.* **34**, 2667 (2009).
- [41] J. D. Caldwell, A. V. Kretinin, Y. Chen, V. Giannini, M. M. Fogler, Y. Francescato, C. T. Ellis, J. G. Tischler, C. R. Woods, A. J. Giles *et al.*, *Nat. Commun.* **5**, 5221 (2014).
- [42] A. K. Kaveev, O. V. Anisimov, A. G. Banshchikov, N. F. Kartenko, V. P. Ulin, and N. S. Sokolov, *J. Appl. Phys.* **98**, 013519 (2005).
- [43] F. Sanjuan and J. O. Tocho, in *Latin America Optics and Photonics Conference* (Optical Society of America, 2012).
- [44] B. Bhoi and S.-K. Kim, *Roadmap for Photon-Magnon Coupling and its Applications* (Academic Press, Cambridge, MA, 2020).
- [45] V. G. Veselago, *Sov. Phys. Usp.* **10**, 509 (1968).
- [46] R. Macêdo and T. Dumelow, *Phys. Rev. B* **89**, 035135 (2014).
- [47] N. R. Anderson and R. E. Camley, *J. Appl. Phys.* **113**, 013904 (2013).
- [48] N. C. Passler and A. Paarmann, *J. Opt. Soc. Am. B* **34**, 2128 (2017).
- [49] N. C. Passler and A. Paarmann, *J. Opt. Soc. Am. B* **36**, 3246 (2019).
- [50] A. Gorodetsky, A. D. Koulouklidis, M. Massaouti, and S. Tzortzakis, *Phys. Rev. A* **89**, 033838 (2014).